

# Correlated order at the tipping point in the kagome metal $\text{CsV}_3\text{Sb}_5$

Received: 11 April 2023

Accepted: 8 December 2023

Published online: 31 January 2024

 Check for updates

Chunyu Guo<sup>1</sup>✉, Glenn Wagner<sup>2</sup>, Carsten Putzke<sup>1</sup>, Dong Chen<sup>3,4</sup>,  
Kaize Wang<sup>1</sup>, Ling Zhang<sup>1</sup>, Martin Gutierrez-Amigo<sup>5,6</sup>, Ion Errea<sup>5,7,8</sup>,  
Maia G. Vergniory<sup>3,7</sup>, Claudia Felser<sup>3</sup>, Mark H. Fischer<sup>2</sup>✉,  
Titus Neupert<sup>2</sup>✉ & Philip J. W. Moll<sup>1</sup>✉

Spontaneously broken symmetries are at the heart of many phenomena of quantum matter and physics more generally. However, determining the exact symmetries that are broken can be challenging due to imperfections such as strain, in particular when multiple electronic orders are competing. This is exemplified by charge order in some kagome systems, where evidence of nematicity and flux order from orbital currents remains inconclusive due to contradictory measurements. Here we clarify this controversy by fabricating highly symmetric samples of a member of this family,  $\text{CsV}_3\text{Sb}_5$ , and measuring their transport properties. We find that a measurable anisotropy is absent at any temperature in the unperturbed material. However, a pronounced in-plane transport anisotropy appears when either weak magnetic fields or strains are present. A symmetry analysis indicates that a perpendicular magnetic field can indeed lead to in-plane anisotropy by inducing a flux order coexisting with more conventional bond order. Our results provide a unifying picture for the controversial charge order in kagome metals and highlight the need for materials control at the microscopic scale in the identification of broken symmetries.

Materials hosting intertwined electronic ordering phenomena provide both an outstanding challenge and opportunity in current condensed matter physics. Phases such as magnetism, charge order, spin textures or superconductivity may cooperate or compete, or merely coexist without much commonality, thus complicating the interpretation of experimental data<sup>1,2</sup>. Disentangling the various order parameters into the most elemental building blocks, separating the primary from secondary orders and understanding their interrelation, is the key to solving their rich puzzle. Complex quantum materials with entangled correlated phases also offer unique electronic response functions: when manipulating one order, one can switch or tune a different one, akin to the unique electromagnetic responses of multiferroics<sup>3,4</sup>.

With the poor performance of ab-initio predictions for such correlated materials, a promising experimental route is to follow structural motifs that either host highly degenerate states or exhibit geometrically frustrated bonds, which are known to commonly host correlated phases at low temperatures. Honeycomb lattices, square nets, perovskite cages or the kagome lattice have been extremely fruitful in this regard<sup>4–8</sup>. The kagome lattice, a net of triangles connected at their vertices, combines both bond frustration and sublattice symmetries and thus has been a successful platform for the design of non-trivial quantum materials<sup>9–16</sup>.

Recently, the kagome family  $(\text{Cs}, \text{K}, \text{Rb})\text{V}_3\text{Sb}_5$  has received significant attention due to the wealth of phases it hosts<sup>16–20</sup>. At high

<sup>1</sup>Max Planck Institute for the Structure and Dynamics of Matter, Hamburg, Germany. <sup>2</sup>Department of Physics, University of Zürich, Zürich, Switzerland.

<sup>3</sup>Max Planck Institute for Chemical Physics of Solids, Dresden, Germany. <sup>4</sup>College of Physics, Qingdao University, Qingdao, China. <sup>5</sup>Centro de Física de Materiales (CSIC-UPV/EHU), Donostia-San Sebastian, Spain. <sup>6</sup>Department of Physics, University of the Basque Country (UPV/EHU), Bilbao, Spain. <sup>7</sup>Donostia International Physics Center, Donostia-San Sebastian, Spain. <sup>8</sup>Fisika Aplikatua Saila, Gipuzkoako Ingeniaritza Eskola, University of the Basque Country (UPV/EHU), Donostia-San Sebastian, Spain. ✉e-mail: [chunyu.guo@mpsd.mpg.de](mailto:chunyu.guo@mpsd.mpg.de); [mark.fischer@uzh.ch](mailto:mark.fischer@uzh.ch); [titus.neupert@uzh.ch](mailto:titus.neupert@uzh.ch); [philip.moll@mpsd.mpg.de](mailto:philip.moll@mpsd.mpg.de)

temperature, these V-based kagome systems are in a centrosymmetric, non-magnetic metallic state, but undergo a charge-density-wave (CDW)-type instability at  $T_{\text{CDW}} \approx 100$  K. Consensus of a  $2 \times 2$  reconstruction in the kagome plane has been reached, yet the exact low-temperature structure and the nature of the out-of-plane reconstruction ( $2 \times 2 \times 2$  versus  $2 \times 2 \times 4$ ) remain to be clarified<sup>21–23</sup>. At even lower temperatures, superconductivity appears at a critical temperature  $T_c \approx 2.5$  K which is enhanced by hydrostatic pressure, anti-correlated with the pressure dependence of the CDW indicating their competitive relationship<sup>24–26</sup>. Beyond this, an impressive set of experiments has demonstrated that an additional phenomenon is happening in this material, often associated with an onset temperature of  $T' \approx 20 - 50$  K, yet the nature and physical influences are under heavy debate, fuelled by openly contradictory experimental results. These experiments include signatures of time-reversal symmetry (TRS) breaking<sup>27–31</sup> and absence thereof<sup>32,33</sup>; electronic nematicity<sup>34–38</sup> and absence thereof<sup>39,40</sup>; and tuneable chirality<sup>41–43</sup> and absence thereof<sup>44</sup>.

The central question is how such carefully conducted experiments on a deceptively simple, stoichiometric material of high crystalline purity yield such contradictory results. Here, we propose, and experimentally demonstrate, that these discrepancies are intrinsically rooted in the strong coupling of the various orders it hosts. This renders this material class extraordinarily sensitive to even weak perturbations, which could safely be ignored in conventional compounds. We demonstrate that in-plane strain and magnetic fields are such sensitive perturbations, yet the material may be highly sensitive to others as well. In the experimental reality, weakest and inhomogeneous residual strains (for example, from crystal defects and sample mounting) are ubiquitous and hard to avoid, while magnetic fields of several Tesla are used in the spirit of non-invasive probes (quantum oscillations, nuclear magnetic resonance, magnetotransport). We propose that shielding crystalline samples from perturbations as much as possible will consolidate the field and lead towards the identification of the correlated ground state without perturbations. The main message of this paper is that the at-first-glance contradictory state of the literature is a feature, not a bug.  $(\text{Cs}, \text{K}, \text{Rb})\text{V}_3\text{Sb}_5$  may well realize the long-standing dream of unusual electronic response functions that directly arise from the near-degeneracy of multiple distinct correlated states.

## Isotropic in-plane transport in zero field

One proposed electronic instability is a spontaneous breaking of the six-fold rotational symmetry of the kagome plane into a two-fold symmetric electronic state<sup>34,35,37</sup>. Such nematic transitions manifest in an emergent transport anisotropy within the plane, which is symmetry-forbidden in a six-fold symmetric kagome plane. To this end, we have machined hexagon-shaped microstructures featuring six contacts, one at each corner of the hexagon, from bulk single crystals using focused-ion-beam (FIB) milling. Great care was taken to align the structure with the in-plane lattice vectors via X-ray diffraction (less than  $0.5^\circ$ ) and to minimize shape deviations to avoid any symmetry lowering due to the structure's shape itself (Fig. 1). Systematic resistance measurements were performed with current applied diagonally across the hexagon and voltage measured along the side, in all three possible configurations. As we will show even weak strains to be critical factors, it is important to remove any residual strain onto the micro-shaped crystal that arises from differential thermal contraction.

Low-strain samples have been achieved in two ways, either by decoupling the structure from the substrate by suspending it freely on ultra-soft  $\text{SiN}_x$  membranes (samples S1 and S4); or by encasing it in an epoxy droplet crafted in such a way that the compressive forces of the contracting soft glue nearly compensate the tensile forces of a hard substrate coupling (sample S3). Both low-stress designs result in an approximately strain-free hexagon at cryogenic temperatures (see Methods section for residual strain estimates and fabrication details)<sup>25</sup>. While in the membrane-based samples the residual strain is

minimized by explicit elastic design<sup>42,45</sup>, their fabrication is complex. The epoxy-based method is inherently less controlled yet has proven to be quite effective in mitigating undesired strain asymmetries. This low-tech approach may also be useful in other techniques, such as scattering methods. To explicitly demonstrate the role of strain, a sample on a purposely mismatched substrate was exposed to strain via differential thermal contraction<sup>46,47</sup>. The effective forces acting on the structure closely resemble a force load pulling on two opposite corners of the otherwise free hexagon. The resulting microscopic strain profile in the hexagon is highly inhomogeneous yet preserves the mirror symmetry along the force direction corroborated by finite element simulations (Methods). The main aim of this strain field is to subject the sample to a weak and complex strain field as it may accidentally arise in various experimental circumstances. Sharp transitions at  $T_{\text{CDW}}$  and  $T_c$ , in perfect agreement with the bulk values, signal the approximately strain-free state of S1, S3 and S4. Our strained sample S2 exhibits broader transitions at a shifted  $T_{\text{CDW}}$  and  $T_c$ , in agreement with their known strain dependence and the broadening due to the strain inhomogeneity<sup>48</sup> (Methods). Our set of samples allows us to probe microscopic signatures of rotational symmetry breaking with a high level of control over the physical state of the sample.

For temperatures above  $T_{\text{CDW}}$ , the resistances measured along three current directions are identical in each of the three samples (Fig. 1), as expected for a six-fold symmetric kagome metal. Interestingly, they remain identical for the low-strain samples S1, S3 and S4 at all temperatures down to  $T_c$  within  $\pm 0.05\%$ . In light of the various contradictory results on the spontaneous symmetry breaking of the electronic structure in  $\text{CsV}_3\text{Sb}_5$ , we emphasize the argumentative power of observing the absence of anisotropy. Electronic anisotropy, if observed, may appear due to intrinsic or extrinsic symmetry breaking, yet its absence constrains us to two possible microscopic scenarios of the underlying electronic state: Either the sample decays into perfectly balanced domain structures as to restore the apparent  $C_6$  symmetry of macroscopically averaging probes such as transport; or it remains fundamentally isotropic in the absence of perturbations. The reproducibility of these results in combination with the  $10\text{--}20\text{ }\mu\text{m}$  size of the hexagon necessitates extremely small domains in the nm-range, as to obtain reliably perfect averaging. Both the high density of energetically costly domain boundaries and the absence of such vastly textured electronic matter in local-probe experiments<sup>21,30</sup> speak against the nano-domain picture, while we note it cannot be excluded from our data.

Importantly, we here discuss only the symmetry of the electronic fluid that governs the transport properties. There is an active debate about the crystalline symmetry describing the accurate ionic positions within the CDW state. The proposed low-temperature structures are mostly orthorhombic, which formally breaks the  $C_6$  symmetry by two main mechanisms: (1) subtle deviations of bond lengths break  $C_6$  within each plane<sup>49</sup>; or (2) stacking  $C_6$  symmetric layers with interlayer phase shifts reduces the global symmetry of the stack to  $C_2$  (ref. 50). The detailed ionic structure is highly important as it reflects the energetics of the reconstructed state over its entire band width. However, our transport study is only sensitive to the details at the chemical potential. The fact that sufficiently decoupled samples show isotropic in-plane responses does not exclude any such structural symmetry breaking effects, it merely evidences that their impact on transport is negligible. This may not be surprising as the structural distortions are so subtle that no consensus on the structure has been reached even with high-resolution X-ray studies.

A different picture appears in the strained case: At  $T_{\text{CDW}}$ , a clearly observable resistivity anisotropy immediately appears. Two directions remain identical within experimental accuracy, while the one along the unidirectional strain direction differs. This is a direct consequence of engineering a complex strain field that remains mirror symmetric along and perpendicular to the applied force. We quantify the

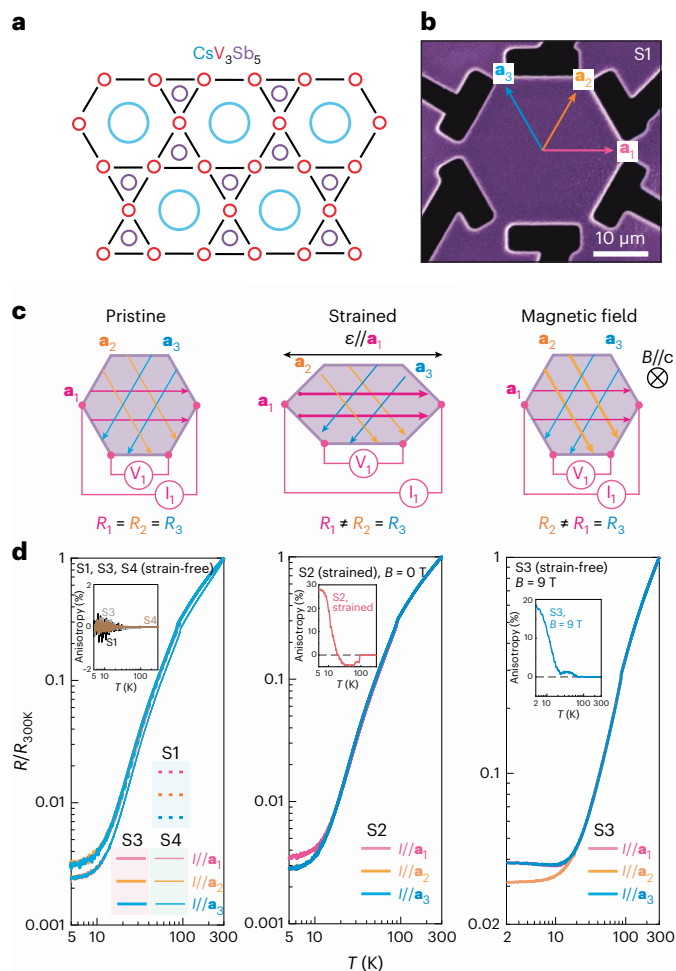


**Fig. 1 | Field- and strain-induced in-plane transport anisotropy in  $\text{CsV}_3\text{Sb}_5$ .** **a**, Detailed setup of tri-directional resistance measurement and possible origin of in-plane anisotropy. **b**, Scanning electron microscopy (SEM) image of device S1. The hexagon of  $\text{CsV}_3\text{Sb}_5$  is fabricated via focused-ion-beam technique with six symmetric contacts. The three equivalent  $a$ -directions of the Kagome plane are noted as  $a_1$ ,  $a_2$  and  $a_3$ , respectively. **c**, Illustration of in-plane electric transport under different conditions. With the application of in-plane strain or out-of-plane magnetic field, the resistances measured along different directions,  $R_i$  ( $i = 1, 2, 3$ ), become anisotropic. Here,  $I$  and  $V$  denote the applied current and the measured voltage, respectively. **d**, Temperature ( $T$ ) dependence of tri-directional resistance for the nearly strain-free devices S1, S3 and S4 in zero field, device S2 under strain and device S3 in the presence of magnetic field ( $B = 9$  T).

experimental anisotropy as the anti-symmetric difference between these two directions,  $(R_1 - R_2)/(R_1 + R_2)$ . This anisotropy remains relatively featureless until it distinctly grows around  $T \approx 30$  K to above 30% at  $T = 5$  K. This sudden growth in the strained sample S2 is accompanied by a sign change of the anisotropy, occurring simultaneously with the various anomalies reported around  $T'$ . These observations are fully consistent with two very recent elastoresistance works on uniaxial strain (cite) that support the non-nematic picture. Using uniaxial strain, a symmetry decomposition revealed a weak response in the nematic channel ( $E_{2g}$ ) yet observed a massive enhancement of the symmetric ( $A_{1g}$ ) response as the samples are cooled through  $T'$ . This suggests the divergent anisotropy under strain likely arises from the strain gradients acting on the  $A_{1g}$  channel. The remarkable non-nematic impact of weak strain fields may be associated with the energetic stability of various close-by structures, such as the orthorhombic ones discussed above. High-precision X-ray studies under uniaxial strain are needed to clarify this point.

## Field- and strain-induced anisotropy

A second, key piece to the puzzle is unveiled by magnetic fields. Previous reports<sup>41</sup> suggested that the rotational symmetry breaking is linked to time-reversal symmetry breaking. Under a static out-of-plane magnetic field  $B_c$ , even strain-free samples exhibit a transport anisotropy, which increases monotonically with increasing magnetic field (Extended Data Fig. 6). For  $B_c = 9$  T, the anisotropy onsets at  $T \approx 70$  K and reaches 20% at low temperature. Similar to the strained samples, the anisotropy increases markedly around  $T' \approx 30$  K. Detailed rotation studies of the magnetic field away from the  $c$  direction have shown no influence, hence we can experimentally exclude a small accidental in-plane field component to be the source of the symmetry breaking (Extended Data Fig. 9). Repeated cooldowns exactly reproduce the state of the sample, speaking against spontaneous symmetry breaking and likely the weak but non-zero residual strain breaks the symmetry statically. Still, in the same sample without a magnetic field no anisotropy is detectable. This behaviour marks out-of-plane magnetic fields  $B_c$  as another crucial tuning parameter for electronic symmetry breaking in  $\text{CsV}_3\text{Sb}_5$ . The state of broken rotational symmetry can be directly controlled by a magnetic field, evidencing the strong coupling between these phenomena. Together, these observations substantiate a consistent experimental picture of an isotropic state in the pristine material that is critically unstable against forming a nematic state under weak perturbations. Indeed, when strain and out-of-plane fields are simultaneously applied, the anisotropy grows even further (Extended Data Fig. 8). Interestingly, high-resolution X-ray studies have not found any evidence for a change in the lattice structure of the CDW state under field<sup>50</sup>, which combined with our results further supports an unconventional type of electronic order.

## Theoretical model of symmetry analysis and strain-field coupling

While in-plane strain can naturally produce an anisotropy by explicitly breaking rotation symmetry, the effect of an out-of-plane field on the transport anisotropy appears, at first glance, surprising. In the following, we elucidate the coupling of strain and magnetic field on a charge-density order parameter in kagome systems within Ginzburg–Landau (GL) theory. For this discussion, we focus on a single kagome layer and are guided by the following experimental observations: (1) there is translational symmetry breaking in the form of a  $2 \times 2$  increase of the size of the (in-plane) unit cell; (2) there is no spontaneous rotational symmetry breaking in the absence of any external perturbation. This restriction will fix the terms of the GL expansion to fourth order in powers of the order parameter; and (3) the magnetic field couples linearly to the system, which restricts the form of the flux phase. We introduce a complex three-component order parameter  $\psi = \Delta + i\Delta'$  defined in Fig. 2a (and transformation properties defined in Supplementary Table 1).  $\Delta$  describes charge bond order while  $\Delta'$  describes flux order and therefore breaks time-reversal symmetry. Importantly, this flux order is even under  $C_2$  symmetry, which is crucial for observation (3). The resulting GL free energy, shown in Methods, is extremely rich<sup>51</sup> and includes not only third-order coupling<sup>49,52–55</sup>, but also a linear coupling of  $\Delta$  with  $\Delta'$  mediated by the out-of-plane field<sup>56</sup>. In the absence of a magnetic field and strain, this free energy leads to the phase diagram shown in Fig. 2b, where from left to right we tune the relative critical temperature of the bond and flux order. As shown in the cuts in Fig. 2c, due to the presence of a third-order term in the free energy, any  $\Delta'$  induces a subsidiary  $\Delta$ , while the converse is not true. Finally, the third-order terms coupling the two order parameters result in an anisotropic solution. Given our observation (2), namely an isotropic order in the absence of external perturbations, we will focus in the following on the scenario 4 of the phase diagram presented in Fig. 2b.



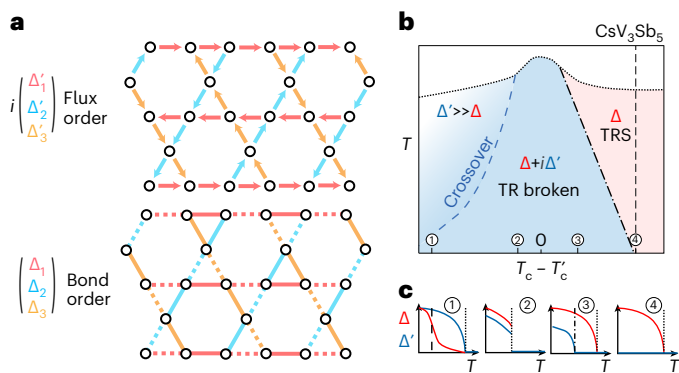


**Fig. 2 | Ginzburg–Landau phase diagram.** **a**, Definition of the three-component order parameters  $\Delta$  (describing real modulation of the bond hopping) and  $\Delta'$  (describing imaginary modulation of the bond hopping, meaning flux order). Both order parameters break translational symmetry and increase the unit cell by  $2 \times 2$ . In the lower panel, solid and dashed lines denote positive and negative values of the bond order parameter, respectively. **b**, Schematic phase diagram of the order parameters  $\Delta$  and  $\Delta'$ . From left to right, we tune the relative critical temperature of  $\Delta$  and  $\Delta'$ . Time-reversal (TR) is broken in the blue region, whereas we have TRS in the pink region. **c**, Order parameters along four vertical cuts through the phase diagram.  $\Delta'$  always induces a subsidiary  $\Delta$ , while the converse is not true.

## Field dependence of anisotropy and phase diagram

The above symmetry considerations on the Ginzburg–Landau level provide a field-strain-temperature phase diagram which reproduces the experimental observations remarkably well. The bond order  $\Delta$  appears below  $T_{\text{CDW}}$  at a (weakly) first-order transition due to the presence of the third-order term. In the absence of a magnetic field or strain, there is no anisotropy, in other words the three components of  $\Delta$  are identical. When a magnetic field is applied,  $\Delta'$  is induced leading to a non-zero anisotropy due to the third-order coupling of  $\Delta$  and  $\Delta'$ . This anisotropy becomes observable at a temperature below the charge-ordering temperature, when the third-order term becomes large enough. The anisotropy is further enhanced by increasing the magnetic field, since that increases the  $\Delta'$  component. In the presence of strain, an anisotropy in  $\Delta$  is induced immediately at the charge-ordering temperature. Furthermore, at a lower temperature  $\Delta'$  can condense as well in the presence of strain, which increases the anisotropy. In both cases, TRS breaking only occurs when  $\Delta'$  is present.

In our scenario, pristine  $\text{CsV}_3\text{Sb}_5$  is thus time-reversal symmetric at any temperature, yet located critically close to the TRS broken phase  $\Delta + i\Delta'$  in the phase diagram (Fig. 3). Applying the magnetic field directly promotes the coupling between the orders and drives an in-plane symmetry breaking at arbitrary low fields, that is without a threshold field. This scenario indeed matches the experimental data: Starting at zero in the absence of field or strain, the anisotropy immediately appears under field and continuously increases up to  $B = 2$  T. At higher magnetic field, the anisotropy continues to grow yet at a slower pace and exhibits pronounced quantum oscillations. While microscopic details such as Landau quantization are naturally not considered in a GL theory, it is remarkable that its general trend continues despite the highly complex transport situation in the microstructure.

Finally, we note that raising the temperature pushes the system towards an isotropic state, which can be straightforwardly mapped out in our experiment (Fig. 3b). The thin isotropic sliver immediately gives rise to an anisotropic state under weakest magnetic fields, which is remarkably similar to the predictions of the GL theory shown in Fig. 3c. This behaviour can be directly rationalized from the phase diagram in Fig. 2b. In such a picture, raising the temperature pushes the system deeper into the isotropic, time-reversal symmetric state.

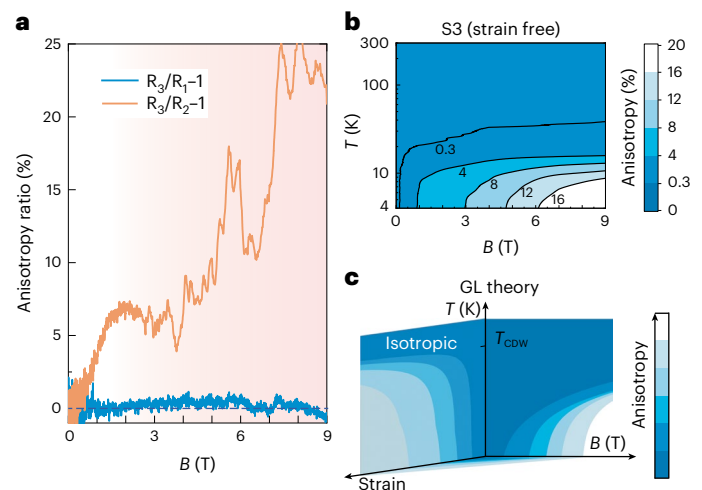


**Fig. 3 | Anisotropic magnetoresistance and characteristic magnetic field scale.** **a**, Field dependence of transport anisotropy in  $\text{CsV}_3\text{Sb}_5$ . **b**, Temperature-field phase diagram of anisotropy. The anisotropy stays zero without applying external magnetic field ( $B = 0$  T) and above  $T \approx 30$  K. **c**, Temperature-field-strain phase diagram reproduced based on Ginzburg–Landau theory, which is consistent with the experimental results displayed in **b**.

## Discussion and outlook

There have been numerous reports on the spontaneous symmetry breaking in  $\text{CsV}_3\text{Sb}_5$  (Fig. 4). Despite the variety of experimental methods, most of the results recognize a six-fold to two-fold in-plane symmetry lowering upon entering the charge-ordered state. In contrast, our measurements of the nearly strain-free samples demonstrate that the electronic transport remains isotropic across the whole temperature range. We argue that this apparent discrepancy is mainly due to the fact that in most experiments, such as angular dependence of magnetoresistance and elasto-transport measurements, magnetic fields and uniaxial strain act as necessary probes of symmetry breaking/lowering. The extreme sensitivity to perturbations amplifies even accidental and in-adverted perturbations that may arise from crystal growth, handling or mounting in the experimental reality. Here, we have clearly demonstrated that these presumably small perturbations act as crucial tuning parameters of the transport anisotropy (Fig. 4). Importantly, there exist two critical temperature scales. Except for the apparent transition temperature  $T_{\text{CDW}}$  at which the strain-induced anisotropy appears exactly, the additional temperature scale  $T'$  stands for the onset of the field-induced anisotropy. This is consistently demonstrated not only by our measurements but also all experiments with external magnetic field or uniaxial strain. These two distinct temperature scales suggest that despite the similar effect between strain and field, the way they couple to the order is different.

Our Ginzburg–Landau discussion provides an intriguing scenario that may reconcile some of the apparent contradictions reported in this field. In this picture,  $\text{CsV}_3\text{Sb}_5$  exhibits an extreme sensitivity of the transport anisotropy due to its critical proximity to the loop-current phase. The anisotropy in the order parameters for cut 4 through the phase diagram in Fig. 2b reproduces successfully the influence of a magnetic field and strain on the temperature dependence of the anisotropy. Hence, our experiments, as well as the published literature, are consistent with a regime where the time-reversal-preserving bond order is dominant, while the TRS-breaking flux order is subdominant and is only induced in the perturbed case.

Our work once more highlights the rich responses and possible advanced functionalities in materials hosting a subtle balance of entangled orders, which can mutually be manipulated. The electronic state within the charge-ordered phase can be readily manipulated by

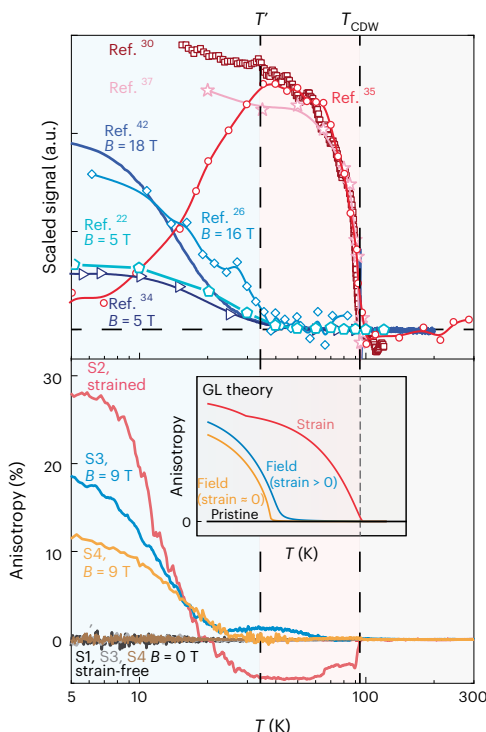


**Fig. 4 | Summary and comparison with previous reports.** Top, summary of the previously reported temperature dependence of anisotropy measured via various methods, including angle-dependent magnetoresistance<sup>22,34</sup>, electric magneto-chiral anisotropy<sup>42</sup>, elasto-resistivity<sup>35</sup>, nuclear magnetic resonance<sup>26</sup>, magneto-optical Kerr effect<sup>30</sup> and optical polarization rotation measurement<sup>37</sup>. Interestingly, all results measured without magnetic field demonstrate that the anisotropy occurs once the charge order is formed. Meanwhile the in-field measurements consistently reveal yet another temperature scale ( $T'$ ) below  $T_{\text{CDW}}$ . Bottom, the anisotropy measured in devices S1, S2, S3 and S4. The field-induced anisotropy occurs only below  $T_{\text{CDW}}$  and displays a gradual increase starts at  $T'$ , while the strain-induced anisotropy onsets exactly at  $T_{\text{CDW}}$ . The inset panel presents the  $T$ -dependent anisotropy of the order parameter under different conditions reproduced by Ginzburg–Landau theory. We choose Ginzburg–Landau parameters corresponding to scenario © in Fig. 2b,c.

weak strain and magnetic fields. Combined with the recently demonstrated chiral transport<sup>42</sup> and optically manipulated chirality<sup>43</sup>, field-, strain- and light-tuned electric diodes become possible, albeit new materials with energy scales above room temperature are necessary for real applications. From a broader perspective, this work sends a beacon of hope into controversial fields which similarly may be unified when previously uncontrolled tuning parameters become controllable in the future, no matter how negligible and irrelevant they may seem at first glance.

## Online content

Any methods, additional references, Nature Portfolio reporting summaries, source data, extended data, supplementary information, acknowledgements, peer review information; details of author contributions and competing interests; and statements of data and code availability are available at <https://doi.org/10.1038/s41567-023-02374-z>.

## References

- Stewart, G. R. Heavy-fermion systems. *Rev. Mod. Phys.* **56**, 755–787 (1984).
- Dagotto, E. Correlated electrons in high-temperature superconductors. *Rev. Mod. Phys.* **66**, 763–840 (1994).
- Tokura, Y., Seki, S. & Nagaosa, N. Multiferroics of spin origin. *Rep. Prog. Phys.* **77**, 076501 (2014).
- Cheong, S.-W. & Mostovoy, M. Multiferroics: a magnetic twist for ferroelectricity. *Nat. Mater.* **6**, 13–20 (2007).
- Yin, J.-X., Lian, B. & Hasan, M. Z. Topological kagome magnets and superconductors. *Nature* **612**, 647–657 (2022).
- Balents, L. Spin liquids in frustrated magnets. *Nature* **464**, 199–208 (2010).
- Keimer, B. & Moore, J. E. The physics of quantum materials. *Nat. Phys.* **13**, 1045–1055 (2017).
- Gardner, J. S., Gingras, M. J. P. & Greedan, J. E. Magnetic pyrochlore oxides. *Rev. Mod. Phys.* **82**, 53–107 (2010).
- Syōzi, I. Statistics of kagomé lattice. *Prog. Theor. Phys.* **6**, 306–308 (1951).
- Kang, M. et al. Topological flat bands in frustrated kagome lattice CoSn. *Nat. Commun.* **11**, 4004 (2020).
- Kang, M. et al. Dirac fermions and flat bands in the ideal kagome metal FeSn. *Nat. Mater.* **19**, 163–169 (2020).
- Yin, J.-X. et al. Quantum-limit Chern topological magnetism in TbMn<sub>6</sub>Sn<sub>6</sub>. *Nature* **583**, 533–536 (2020).
- Yin, J.-X. et al. Giant and anisotropic many-body spin–orbit tunability in a strongly correlated kagome magnet. *Nature* **562**, 91–95 (2018).
- Ye, L. et al. Massive Dirac fermions in a ferromagnetic kagome metal. *Nature* **555**, 638–642 (2018).
- Howard, S. et al. Evidence for one-dimensional chiral edge states in a magnetic Weyl semimetal Co<sub>3</sub>Sn<sub>2</sub>S<sub>2</sub>. *Nat. Comm.* **12**, 4269 (2021).
- Ortiz, B. R. et al. New kagome prototype materials: discovery of KV<sub>3</sub>Sb<sub>5</sub>, RbV<sub>3</sub>Sb<sub>5</sub>, and CsV<sub>3</sub>Sb<sub>5</sub>. *Phys. Rev. Mater.* **3**, 094407 (2019).
- Ortiz, B. R. et al. CsV<sub>3</sub>Sb<sub>5</sub>: A  $Z_2$  topological kagome metal with a superconducting ground state. *Phys. Rev. Lett.* **125**, 247002 (2020).
- Kang, M. et al. Twofold van Hove singularity and origin of charge order in topological kagome superconductor CsV<sub>3</sub>Sb<sub>5</sub>. *Nat. Phys.* **18**, 301–308 (2022).
- Denner, M. M., Thomale, R. & Neupert, T. Analysis of charge order in the kagome metal AV<sub>3</sub>Sb<sub>5</sub> (A = K, Rb, Cs). *Phys. Rev. Lett.* **127**, 217601 (2021).
- Neupert, T., Denner, M. M., Yin, J.-X., Thomale, R. & Hasan, M. Z. Charge order and superconductivity in kagome materials. *Nat. Phys.* **18**, 137–143 (2022).
- Zhao, H. et al. Cascade of correlated electron states in a kagome superconductor CsV<sub>3</sub>Sb<sub>5</sub>. *Nature* **599**, 216–221 (2021).
- Chen, H. et al. Roton pair density wave in a strong-coupling kagome superconductor. *Nature* **599**, 222–228 (2021).
- Chen, Q., Chen, D., Schnelle, W., Felser, C. & Gaulin, B. D. Charge density wave order and fluctuations above  $T_{\text{CDW}}$  and below superconducting  $T_c$  in the kagome metal CsV<sub>3</sub>Sb<sub>5</sub>. *Phys. Rev. Lett.* **129**, 056401 (2022).
- Wang, Q. et al. Charge density wave orders and enhanced superconductivity under pressure in the kagome metal CsV<sub>3</sub>Sb<sub>5</sub>. *Adv. Mat.* **33**, 2102813 (2021).
- Du, F. et al. Pressure-induced double superconducting domes and charge instability in the kagome metal KV<sub>3</sub>Sb<sub>5</sub>. *Phys. Rev. B* **103**, L220504 (2021).
- Zheng, L. et al. Emergent charge order in pressurized kagome superconductor CsV<sub>3</sub>Sb<sub>5</sub>. *Nature* **611**, 682–687 (2022).
- Mielke, C. et al. Time-reversal symmetry-breaking charge order in a kagome superconductor. *Nature* **602**, 245–250 (2022).
- Yu, L. et al. Evidence of a hidden flux phase in the topological kagome metal CsV<sub>3</sub>Sb<sub>5</sub>. Preprint at <https://doi.org/10.48550/arXiv.2107.10714> (2021).
- Hu, Y. et al. Time-reversal symmetry breaking in charge density wave of CsV<sub>3</sub>Sb<sub>5</sub> detected by polar Kerr effect. Preprint at <https://doi.org/10.48550/arXiv.2208.08036> (2022).
- Xu, Y. et al. Three-state nematicity and magneto-optical Kerr effect in the charge density waves in kagome superconductors. *Nat. Phys.* **18**, 1470–1475 (2022).

31. Wang, J., Farhang, C., Ortiz, B. R., Wilson, S. D. & Xia, J. Resolving the discrepancy between MOKE measurements at 1550-nm wavelength on Kagome Metal  $\text{CsV}_3\text{Sb}_5$ . Preprint at <https://doi.org/10.48550/arXiv.2301.08853> (2023).
32. Saykin, D. R. et al. High resolution polar Kerr effect studies of  $\text{CsV}_3\text{Sb}_5$ : tests for time reversal symmetry breaking below the charge order transition. *Phys. Rev. Lett.* **131**, 016901 (2022).
33. Li, H. et al. No observation of chiral flux current in the topological kagome metal  $\text{CsV}_3\text{Sb}_5$ . *Phys. Rev. B* **105**, 045102 (2022).
34. Xiang, Y. et al. Twofold symmetry of c-axis resistivity in topological kagome superconductor  $\text{CsV}_3\text{Sb}_5$  with in-plane rotating magnetic field. *Nat. Commun.* **12**, 6727 (2021).
35. Nie, L. et al. Charge-density-wave-driven electronic nematicity in a kagome superconductor. *Nature* **604**, 59–64 (2022).
36. Wulferding, D. et al. Emergent nematicity and intrinsic versus extrinsic electronic scattering processes in the kagome metal  $\text{CsV}_3\text{Sb}_5$ . *Phys. Rev. Res.* **4**, 023215 (2022).
37. Wu, Q. et al. Simultaneous formation of two-fold rotation symmetry with charge order in the kagome superconductor  $\text{CsV}_3\text{Sb}_5$  by optical polarization rotation measurement. *Phys. Rev. B* **106**, 205109 (2022).
38. Asaba, T. et al. Evidence for an odd-parity nematic phase above the charge density wave transition in kagome metal  $\text{CsV}_3\text{Sb}_5$ . Preprint at <https://doi.org/10.48550/arXiv.2309.16985> (2023).
39. Liu, Z. et al. Absence of nematic instability in the kagome metal  $\text{CsV}_3\text{Sb}_5$ . Preprint at <https://doi.org/10.48550/arXiv.2309.14574> (2023).
40. Frachet, M. et al. Colossal c-axis response and lack of rotational symmetry breaking within the kagome plane of the  $\text{CsV}_3\text{Sb}_5$  superconductor. Preprint at <https://doi.org/10.48550/arXiv.2310.06102> (2023).
41. Jiang, Y.-X. et al. Unconventional chiral charge order in kagome superconductor  $\text{KV}_3\text{Sb}_5$ . *Nat. Mat.* **20**, 1353–1357 (2021).
42. Guo, C. et al. Switchable chiral transport in charge-ordered kagome metal  $\text{CsV}_3\text{Sb}_5$ . *Nature* **611**, 461–466 (2022).
43. Xing, Y. et al. Optical manipulation of the charge density wave state in  $\text{RbV}_3\text{Sb}_5$ . Preprint at <https://doi.org/10.48550/arXiv.2308.04128> (2023).
44. Li, H. et al. Rotation symmetry breaking in the normal state of a kagome superconductor  $\text{KV}_3\text{Sb}_5$ . *Nat. Phys.* **18**, 265–270 (2022).
45. Huang, X. et al. Three-dimensional Fermi surfaces from charge order in layered  $\text{CsV}_3\text{Sb}_5$ . *Phys. Rev. B* **106**, 064510 (2022).
46. Bachmann, M. D. et al. Spatial control of heavy-fermion superconductivity in  $\text{CeIrIn}_5$ . *Science* **366**, 221–226 (2019).
47. van Delft, M. R. et al. Controlling superconductivity of  $\text{CeIrIn}_5$  microstructures by substrate selection. *Appl. Phys. Lett.* **120**, 092601 (2022).
48. Qian, T. et al. Revealing the competition between charge density wave and superconductivity in  $\text{CsV}_3\text{Sb}_5$  through uniaxial strain. *Phys. Rev. B* **104**, 144506 (2021).
49. Kautzsch, L. et al. Structural evolution of the kagome superconductors  $\text{AV}_3\text{Sb}_5$  (A = K, Rb, and Cs) through charge density wave order. *Phys. Rev. Mater.* **7**, 024806 (2023).
50. Stahl, Q. et al. Temperature-driven reorganization of electronic order in  $\text{CsV}_3\text{Sb}_5$ . *Phys. Rev. B* **105**, 195136 (2022).
51. Wagner, G., Guo, C., Moll, P. J. W., Neupert, T. & Fischer, M. H. Phenomenology of bond and flux orders in kagome metals. *Phys. Rev. B* **108**, 125136 (2023).
52. Christensen, M. H., Birol, T., Andersen, B. M. & Fernandes, R. M. Theory of the charge density wave in  $\text{AV}_3\text{Sb}_5$  kagome metals. *Phys. Rev. B* **104**, 214513 (2021).
53. Christensen, M. H., Birol, T., Andersen, B. M. & Fernandes, R. M. Loop currents in  $\text{AV}_3\text{Sb}_5$  kagome metals: multipolar and toroidal magnetic orders. *Phys. Rev. B* **106**, 144504 (2022).
54. Grandi, F., Consiglio, A., Sentef, M. A., Thomale, R. & Kennes, D. M. Theory of nematic charge orders in kagome metals. *Phys. Rev. B* **107**, 155131 (2023).
55. Han, T., Che, J., Ye, C. & Huang, H. Landau analysis on the physical properties of the kagome superconductor  $\text{CsV}_3\text{Sb}_5$ . *Crystals* **13**, 321 (2023).
56. Tazai, R., Yamakawa, Y. & Kontani, H. Drastic magnetic-field-induced chiral current order and emergent current-bond-field interplay in kagome metal  $\text{AV}_3\text{Sb}_5$  (A=Cs,Rb,K). Preprint at <https://doi.org/10.48550/arXiv.2303.00623> (2023).

**Publisher's note** Springer Nature remains neutral with regard to jurisdictional claims in published maps and institutional affiliations.

**Open Access** This article is licensed under a Creative Commons Attribution 4.0 International License, which permits use, sharing, adaptation, distribution and reproduction in any medium or format, as long as you give appropriate credit to the original author(s) and the source, provide a link to the Creative Commons license, and indicate if changes were made. The images or other third party material in this article are included in the article's Creative Commons license, unless indicated otherwise in a credit line to the material. If material is not included in the article's Creative Commons license and your intended use is not permitted by statutory regulation or exceeds the permitted use, you will need to obtain permission directly from the copyright holder. To view a copy of this license, visit <http://creativecommons.org/licenses/by/4.0/>.

© The Author(s) 2024



## Methods

### Crystal synthesis and characterization

$\text{CsV}_3\text{Sb}_5$  crystallizes in the hexagonal structure with the  $P6/mmm$  space group. It contains layers of kagome planes formed by the V atoms. Following a self-flux procedure described in ref. 17, we obtained plate-like single crystals with typical dimensions of  $2 \times 2 \times 0.04 \text{ mm}^3$ .

The micro-devices S1, S2, S3 and S4 are fabricated using the focused-ion-beam (FIB) technique (Extended Data Fig. 1). First, three slabs called lamellae are obtained from the same piece of bulk sample, and the plane of each lamella is aligned accurately to the kagome plane with less than  $\pm 0.5^\circ$  misalignment. For device S1, the lamella is transferred in-situ by a micro-manipulator and welded to a gold-coated (Au:100 nm)  $\text{SiN}_x$  membrane chip via Pt-deposition. The membrane window is about 200 by 200  $\mu\text{m}$ , and its thickness is 100 nm. Soft meander-shaped springs are later fabricated to relax the thermal contraction strain with a typical spring constant  $\sim 100 \text{ N m}^{-1}$ . Meanwhile for both S2 and S3 the lamellae are transferred ex-situ and glued down to a sapphire substrate with prepatterned gold electrodes. All devices are exposed to a low-voltage (2 kV) Xe ion beam cleaning as the final fabrication step to reduce the thickness of FIB-damaged amorphous layer. After the fabrication of device S3, a small glue droplet of red araldite is added on top of the device via a thin wooden tip to reduce and homogenize the uniaxial strain observed in S2. The added glue thickness is about 30  $\mu\text{m}$ . Since the thermal expansion coefficient of the glue is substantially larger than the device, it results in a compressive strain across the device and therefore compensates the tensile differential strain at low temperature. Furthermore, to demonstrate the reproducibility of the experimental results, another membrane-based device S4 was fabricated on a lamella cut from a different  $\text{CsV}_3\text{Sb}_5$  crystal. Despite the slight difference in the exact temperature dependence of resistivity, the isotropic in-plane transport is consistently revealed (Fig. 1d).

To ensure that no apparent misalignment or change of crystalline structure is induced during the fabrication process, we have performed single crystal X-ray diffraction measurements of the bulk sample before FIB fabrication and the device S4 after the resistance measurements (Extended Data Fig. 2). This helps us to minimize the misalignment of crystalline axis down to less than  $0.5^\circ$ . The detailed comparison of crystalline lattice parameters demonstrates the unchanged crystalline structure after the fabrication process. Note that the small silicon opening window of the membrane device S4 limits the angle range of X-ray detection, rendering its Laue indexes weaker than the bulk sample.

Resistance measurements were performed using the resistivity measurement option in a Dynacool PPMS system with a maximal magnetic field of 9 T and base temperature of 2 K. The configurations of in-plane resistance measurements are illustrated in Fig. 1. For each current configuration, the voltages were measured along both sides of the device to ensure the current homogeneity. For all measurements a low AC current of 100  $\mu\text{A}$  is used to avoid Joule heating. All temperature-dependence measurements were performed at a low sweeping rate of  $1 \text{ K min}^{-1}$ . For all devices, the resistance varies from 0.2  $\Omega$  to 0.2 m $\Omega$  with a high residual resistivity ratio (RRR) above 300 (Extended Data Fig. 3). The high RRR and the clear observation of Shubnikov-de Haas oscillations demonstrate the unchanged crystalline quality of all devices after FIB fabrication as well as the irrelevance of FIB-damaged amorphous layer in the measurements of highly conductive materials.

To exclude the role of in-plane fields and misalignment of the magnetic field, full two-axis rotations were achieved via a standard PPMS rotator probe: one angle  $\theta$  is set by a stepper motor while the angle  $\phi$  is controlled by manual positioning outside of the cryostat. The exact angle is determined using the image taken under an optical microscope.

### Detailed analysis of strain effect

Each device displays a strain profile due to the different geometry. Devices S1 and S4 are membrane-based devices with micro-springs

fabricated by FIB. These soft springs strongly compensate the thermal contraction strain which therefore results in a nearly strain-free situation (Extended Data Fig. 4). On the contrary, device S2 is directly attached to the sapphire substrate with glue. The mismatch of thermal contraction coefficient between  $\text{CsV}_3\text{Sb}_5$  and sapphire results in a significant uniaxial strain. The uniaxial strain strongly influences the transport anisotropy of the device. Device S3 features the same setup with S2 yet a glue droplet is applied onto the top after the fabrication process. The larger thermal contraction coefficient of the glue results in a partially compensated and homogenized strain pattern. As a consequence, only the device S2 displays clear anisotropy after the charge order is formed while both S1 and S3 display no anisotropy at zero field down to low temperature. The thermal differential strain of each microstructure can be consistently checked by the charge-ordering temperature. The membrane-mount devices S1 and S4 display identical  $T_{\text{CDW}}$  as expected, while an apparent change of  $T_{\text{CDW}}$  for device S2 demonstrates the presence of tensile strain across the device. According to previous reports<sup>48</sup>, the estimated effective strain is around 0.12%. The broadening of the transition temperature also indicates an inhomogeneous strain distribution. The visible shift of  $T_{\text{CDW}}$  in device S3 is partially attributed to the homogenized pressure effect because of the glue droplet applied, causing an overestimation of tensile strain value displayed in Extended Data Fig. 4c.

To further demonstrate the strain profile difference, we also performed a finite element simulation using COMSOL multiphysics software (Extended Data Fig. 5). For the on-chip device S2, a strong and highly inhomogeneous in-plane strain component is obtained and the average value across the middle hexagon is estimated to be  $\sim 0.25\%$ . With the application of the glue droplet, the in-plane strain is clearly suppressed, and the averaged value is only  $\sim 0.04\%$ . Most importantly, the simulation results of the membrane-based device demonstrate a significant in-plane strain suppression as the averaged value is reduced to less than 0.002%, which is two orders of magnitude smaller than device S2. These results further demonstrate a modulation of in-plane strain profile due to the different device geometry.

### Temperature dependence of transport anisotropy and magnetoresistance

The temperature dependence of the in-plane anisotropy under various magnetic fields (Extended Data Fig. 6) demonstrates its strengthening in field. Not only the absolute value increases, also the onset at which the anisotropy becomes visible increases from 25 K at  $B = 1 \text{ T}$  to 70 K at  $B = 9 \text{ T}$ . Note that this temperature dependence is slightly different from the uniaxial strain case as the anisotropy never becomes fully negative. Compared to S3, device S4 displays a smaller anisotropy at low temperature, most probably due to the difference in strain distribution across the device (Extended Data Fig. 6). This demonstrates a direct coupling between the magnetic field and uniaxial strain, consistent with the prediction by the Ginzburg–Landau theory.

The temperature dependence of the magnetoresistance (MR),  $[R(B)/R(0)]$ , is consistent with previous report as it only becomes significant below  $T_{\text{CDW}}$  (Extended Data Fig. 7)<sup>45</sup>. This indicates the Fermi surface reconstruction due to charge ordering, which leads to the appearance of three-dimensional Fermi pockets and consequently the visible magnetoresistance.

This trend continues when both magnetic field and strains are applied simultaneously. The transport anisotropy of device S2 increases when an external magnetic field of  $B = 1 \text{ T}$  is applied (Extended Data Fig. 8).

### Angular dependence of magnetoresistance

In magnetotransport experiments, field misalignment is a common extrinsic source of lowered apparent symmetry. In our case, to examine

the effect of field misalignment away from the  $c$  direction on the anisotropic transport we report, an extensive angular dependence of MR measurements have been performed with not one but two rotational axes to cover all possible field directions in three-dimensional space (Extended Data Fig. 9). The rotation from out-of-plane to in-plane direction with the angle  $\theta$  is controlled by the rotator motor on the PPMS horizontal rotator with a  $0.5^\circ$  per step resolution. Meanwhile, the in-plane rotation is done by manually altering the position of the device on the rotator puck. For each measurement a high-resolution image is taken via the optical microscope, and the angle  $\varnothing$  is determined digitally using the alignment marker on the image. With external field  $B = 9$  T, except for the clear dip around  $\theta \approx 180^\circ$ , note that at smaller  $\varnothing$ , the MR measured with  $\parallel \mathbf{a}_2$  is larger than the MR for other two current directions. The difference is gradually suppressed and becomes invisible for  $\varnothing$  larger than  $46^\circ$ .

This behaviour is closely related to the admixture of low longitudinal MR set by the angle between the magnetic field and current directions, which explains the variation of MR difference with in-plane rotation. The dip at  $\theta \approx 180^\circ$ , however, is insensitive to in-plane rotation, as it can be consistently observed in all  $\varnothing$  angles. This demonstrates an intrinsically lower magnetoresistance for  $\parallel \mathbf{a}_2$  with  $B \parallel c$ , which is insensitive to misalignment between the sample and magnetic field. In particular, it is not tuned by the residual in-plane magnetic field component. This point can be further elaborated by the results measured at a lower magnetic field ( $B = 1$  and  $4$  T) as a clear difference between  $\parallel \mathbf{a}_2$  and other directions is observed over a wide range of angle  $\theta$ . This is mainly due to the reduced effect of the longitudinal MR component and smaller quantum oscillation amplitude at a lower magnetic field. Thus we conclude that the observed in-plane anisotropy is an intrinsic property of  $\text{CsV}_3\text{Sb}_5$  which is robust against extrinsic perturbations such as misalignment.

### Field dependence of magnetoresistance

The magnetoresistance has been measured along all three different current directions. The resistance for  $\parallel \mathbf{a}_2$  displays a clear difference compared to the other two curves, from which the anisotropy displayed in Fig. 3a was extracted. Meanwhile all curves display a shoulder-like feature at  $B \approx 1.6$  T (Extended Data Fig. 10), consistent with previous reports<sup>45</sup>. This feature corresponds well with a plateau in the field dependence of transport anisotropy (Fig. 3a).

### Data availability

Data that support the findings of this study are available at Zenodo with the access link: <https://doi.org/10.5281/zenodo.10076422>. Source data are provided with this paper.

### Code availability

Code that support the findings of this study are available at Zenodo with the access link: <https://doi.org/10.5281/zenodo.10076422>.

## Acknowledgements

This work was funded by the European Research Council (ERC) under the European Union's Horizon 2020 research and innovation programme (MiTopMat—grant agreement No. 715730 and PARATOP—grant agreement No. 757867). This project received funding by the Swiss National Science Foundation (Grants No. PPOOP2\_176789). M.G.V., I. E. and M.G.A. acknowledge the Spanish Ministerio de Ciencia e Innovación (grant PID2019-109905GB-C21). M.G.V., C.F. and T.N. acknowledge support from FOR 5249 (QUAST) lead by the Deutsche Forschungsgemeinschaft (DFG, German Research Foundation). M.G.V. acknowledges partial support to European Research Council grant agreement no. 101020833. This work has been supported in part by Basque Government grant IT979-16. This work was also supported by the European Research Council Advanced Grant (No. 742068) TOPMAT, the Deutsche Forschungsgemeinschaft (Project-ID No. 247310070) SFB 1143 and the DFG through the Würzburg-Dresden Cluster of Excellence on Complexity and Topology in Quantum Matter ct.qmat (EXC 2147, Project-ID No. 390858490).

## Author contributions

Crystals were synthesized and characterized by D.C. and C.F. The experiment design, FIB microstructuring and magnetotransport measurements were performed by C.G., C.P. and P.J.W.M. G.W., M.H.F. and T.N. developed and applied the general theoretical framework, and the analysis of experimental results was performed by C.G., C.P., K.W., L.Z. and P.J.W.M. All authors were involved in writing the paper.

## Funding

Open access funding provided by Max Planck Society.

## Competing interests

The authors declare no competing interests.

## Additional information

**Extended data** is available for this paper at <https://doi.org/10.1038/s41567-023-02374-z>.

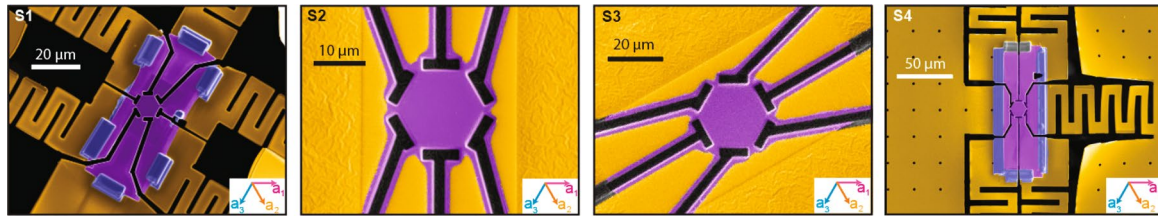
**Supplementary information** The online version contains supplementary material available at <https://doi.org/10.1038/s41567-023-02374-z>.

**Correspondence and requests for materials** should be addressed to Chunyu Guo, Mark H. Fischer, Titus Neupert or Philip J. W. Moll.

**Peer review information** *Nature Physics* thanks Jiun-Haw Chu, Sheng Ran and the other, anonymous, reviewer(s) for their contribution to the peer review of this work.

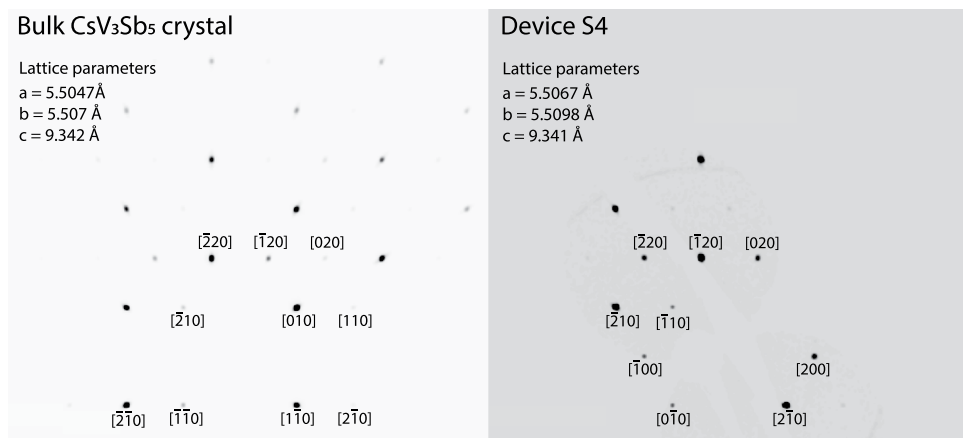
**Reprints and permissions information** is available at [www.nature.com/reprints](http://www.nature.com/reprints).





**Extended Data Fig. 1 | Scanning electron microscope (SEM) images of device S1, S2, S3 and S4.** S1 and S4 are membrane devices with reduced differential thermal contraction strain, while S2 is glued down to a sapphire substrate, the coupling between the substrate and sample results in the non-negligible uni-axial

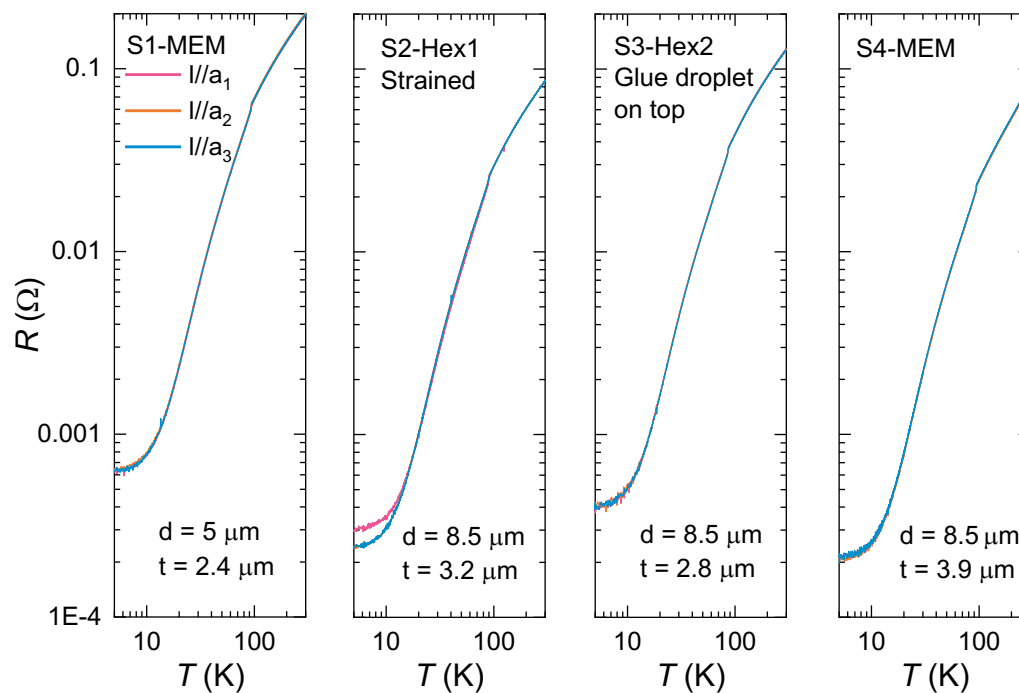
strain at low temperature. S3 is a similar device with S2, yet after taking the SEM image, a glue droplet is applied on top of the device to reduce uniaxial strain at low temperature.



**Extended Data Fig. 2 | X-ray diffraction pattern of bulk sample and device S4.**

To check the crystalline alignment of the microstructure, we have performed X-ray diffraction measurements on both the bulk single crystal before FIB-fabrication (left) and the micro-structured device (right). The comparison demonstrates no change of crystalline structure. Note that as the substrate around the microstructure becomes a shadow for X-ray at certain angle

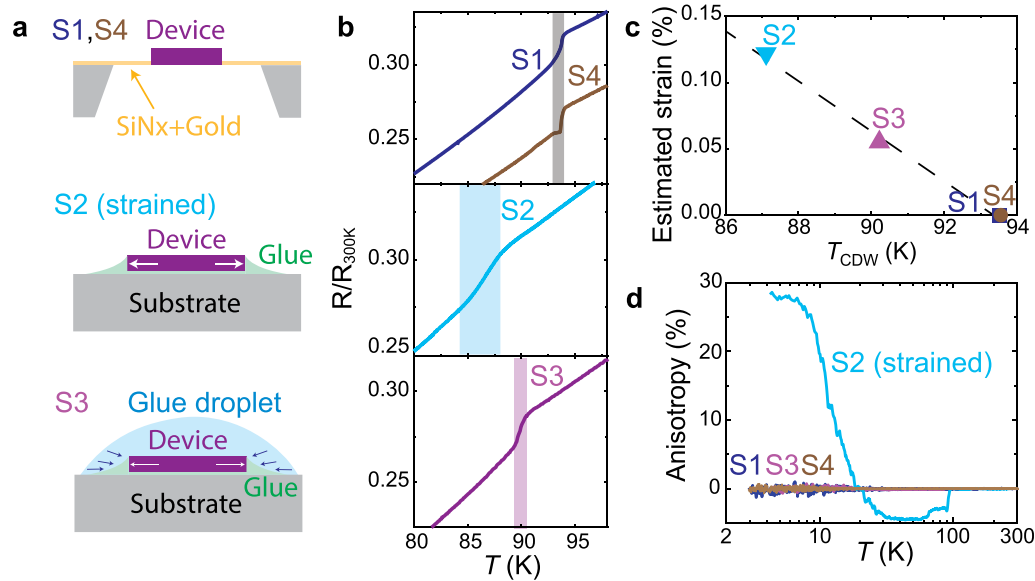
range, the numbers of diffraction peaks are slightly reduced. The full angle X-ray measurement is accompanied by a video taken by the optical camera which records the motion of rotation in one degree step. We found that the crystallographic  $c$ -axis is aligned with the surface norm of the silicon substrate, demonstrating nearly zero misalignment. Based on the accuracy of such determination, the misalignment of crystalline axis is restricted to  $\pm 0.5$  degree.



**Extended Data Fig. 3 | Temperature-dependent resistance of all four different devices.**  $d$  and  $t$  stand for the edge length and thickness of the hexagon respectively. For S1, S3 and S4, the  $T$ -dependence of resistance measured along different axis is nearly identical with each other. This demonstrates the

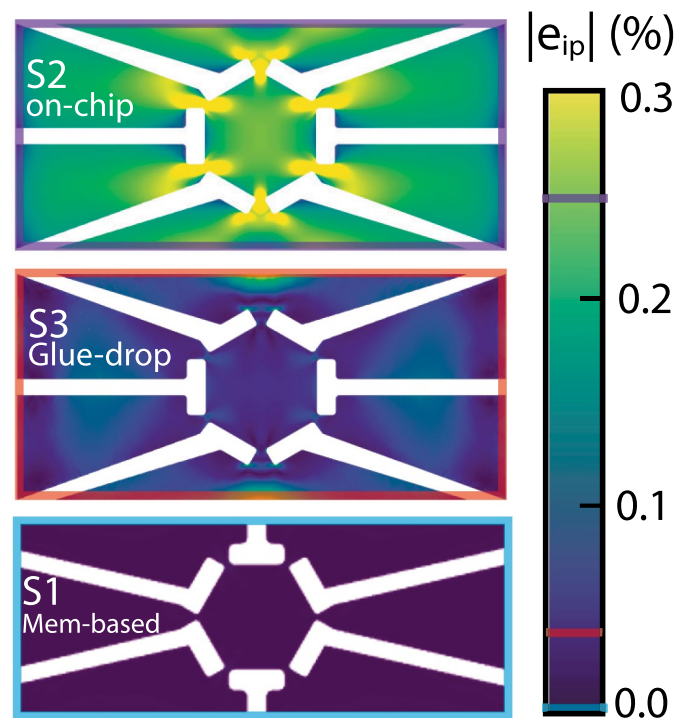
isotropic in-plane transport in these two devices. Meanwhile, for sample S2, the resistance measured with current along  $a_1$  displays a clear difference with the results measured along other current directions. This difference stands for the electronic anisotropy which increases with decreasing temperature.



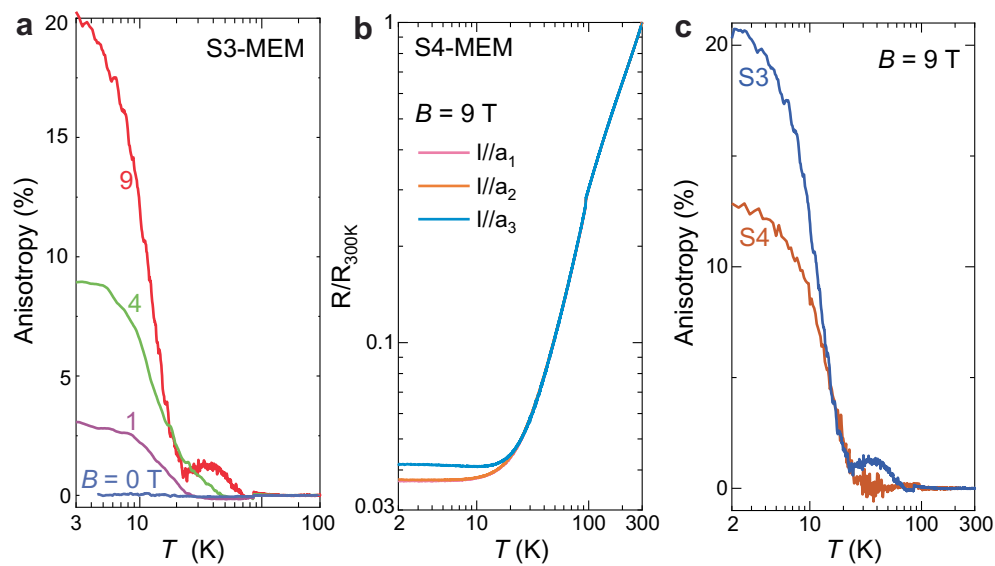


**Extended Data Fig. 4 | Strain analysis and T-dependence of transport anisotropy.** (a) displays the detailed setup of each devices. The uniaxial strain due to differential thermal contraction is suppressed by the soft membrane spring in device S1, S4 and compensation of glue droplet in device S3. (b) Temperature dependence of resistivity near the charge density wave transition. Due to strain inhomogeneity, the transition is shifted to lower temperatures and

becomes broader. (c) Estimating tensile strains of different devices based on the measured charge ordering temperatures. (d) Temperature dependence of transport anisotropy of all devices. S1, S3 and S4 display negligible anisotropy down to low temperature, while the strained sample S2 shows clear anisotropy which appears at the charge-density-wave transition and gets more pronounced at base temperature.



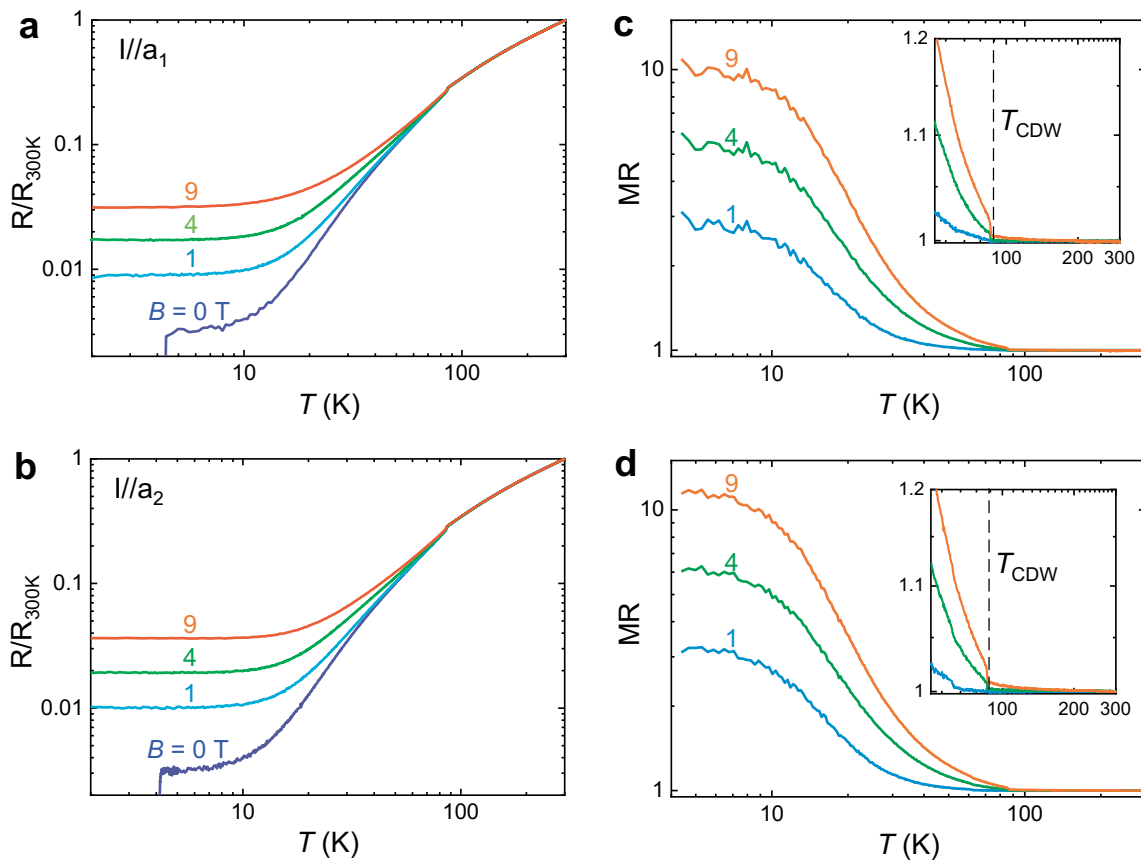
**Extended Data Fig. 5 | COMSOL simulation of uniaxial strain.** Finite element simulation of strain distribution of device S1, S2 and S3 based on COMSOL multiphysics. The results display a dominant uniaxial strain component along the long side of the lamella.



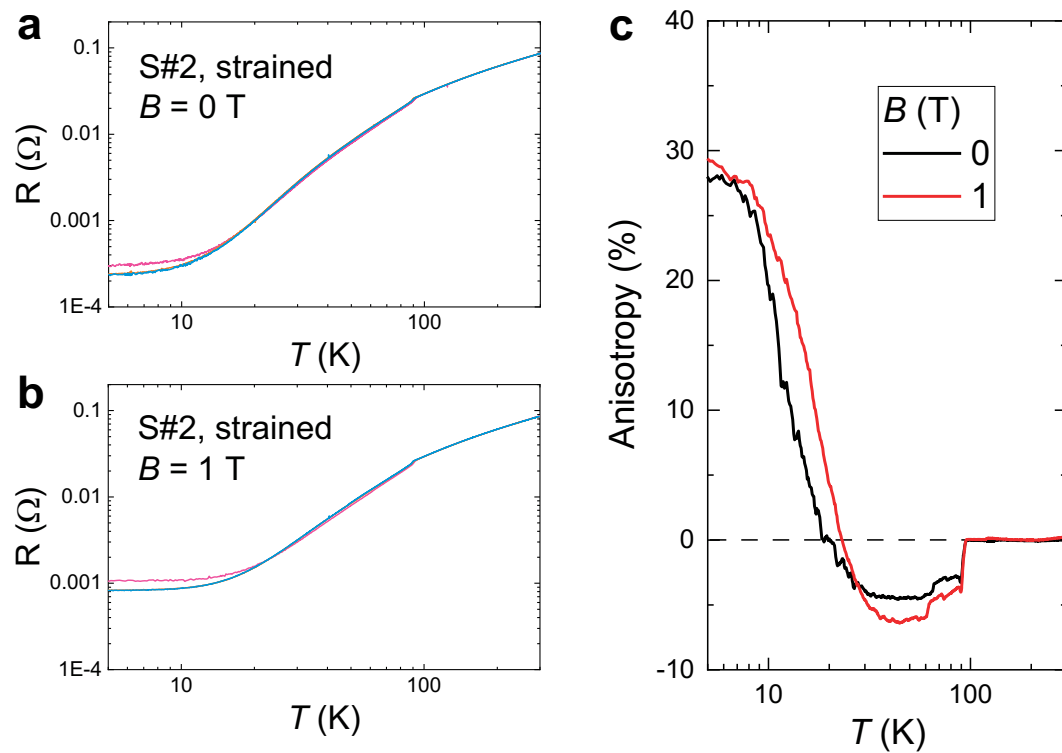
**Extended Data Fig. 6 | Field-induced transport anisotropy of device S3 and S4.** (a)  $T$ -dependent transport anisotropy of S3 measured at different magnetic fields. The low temperature anisotropy increases strongly with increasing magnetic field. (b)  $T$ -dependent resistivity of S4 measured at different current

directions with an external magnetic field of 9 T. (c) Transport anisotropy at 9 T for both S3 and S4. The difference is likely due to the difference in uniaxial strain across the device.

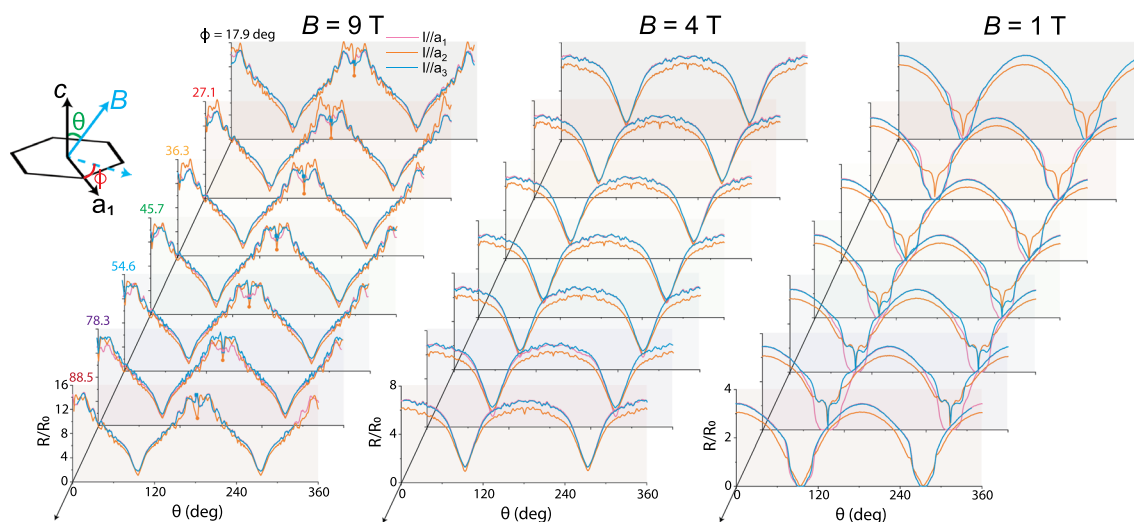




**Extended Data Fig. 7 | T-dependence of magnetoresistance for S3.** (a) and (b) display the T-dependence of resistance measured at various magnetic fields with current along  $a_1$  and  $a_2$  respectively. The magnetoresistance ratio  $[R(B)/R_0]$  for both current directions are presented in (c) and (d) respectively. It is clear that MR only becomes significant below the charge-ordering temperature.

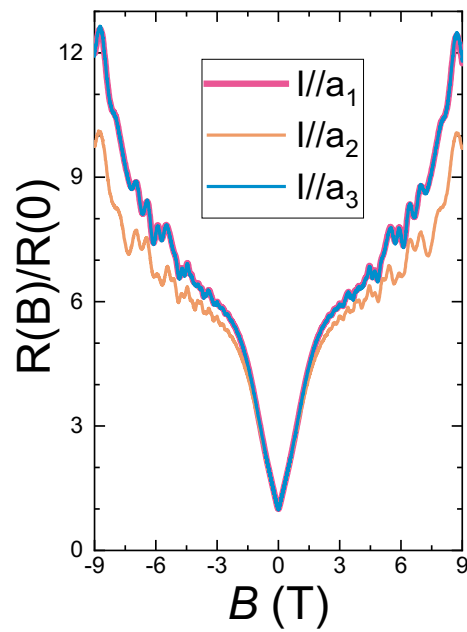


**Extended Data Fig. 8 | T-dependent resistance and in-plane anisotropy of S2 at  $B = 0$  and 1 T.** (a) and (b) present  $T$ -dependence of directional resistance measured at zero field and  $B = 1$  T. The anisotropy due to strain is slightly enhanced by magnetic field, as shown in (c).



**Extended Data Fig. 9 | Angular dependence of MR (AMR) for S3.** AMR measured with spherical rotation and different magnetic fields. The difference between  $I//a_2$  and other two current directions can be clearly seen for all  $\phi$ , demonstrating the intrinsic nature of such behavior.





**Extended Data Fig. 10 | Magnetoresistance along different directions.** Field dependence of magnetoresistance measured along all three different current directions at  $T = 2$  K in device S3. The results measured with  $I//a_1$  and  $I//a_3$  overlaps exactly with each other, yet deviates clearly with  $I//a_2$ . All magnetoresistances display a shoulder-like feature at around  $B \approx 1.6$  T.